

**In Silico Investigation of the
Light Transmission Profiles
of Sand-Textured Soils**

by

Mark Iwanchyshyn

A thesis
presented to the University of Waterloo
in fulfillment of the
thesis requirement for the degree of
Master of Mathematics
in
Computer Science

Waterloo, Ontario, Canada, 2020

© Mark Iwanchyshyn 2020

Author's Declaration

I hereby declare that I am the sole author of this thesis. This is a true copy of the thesis, including any required final revisions, as accepted by my examiners.

I understand that my thesis may be made electronically available to the public.

Abstract

Sand-textured soils are found in a wide range of landscapes, from dune fields to coastal areas. The quantification of light penetration through these soils, particularly considering possible variations in the presence of water in their pore space, is of considerable interest not only for remote sensing applications, but also for agricultural, ecological and geophysical studies. Despite its relevance, however, the literature on this topic is still scarce. Moreover, the available light penetration (transmittance) datasets for these soils are affected by experimental and modeling limitations. These include, for instance, the use of samples with morphological and mineralogical characteristics markedly different from those of naturally occurring sand-textured soils. In the investigation described in this thesis, we demonstrate the importance of properly accounting for the iron oxide contents and grain (particle) distributions of these soils in applied research initiatives linked to their spectral responses, notably in the 400 to 1000 *nm* region of the light spectrum. In order to overcome the limitations outlined above and strengthen the current knowledge in this area, we employed a predictive simulation platform supported by measured data. This platform has as its central component a first-principles light transport model for particulate materials whose implementation has been substantially enhanced during this work. Thus, using this platform, we were able to perform controlled *in silico* experiments on selected representative samples of these soils by systematically varying their water content, their thickness and the angle of light incidence. Our findings provide an original multi-faceted assessment, both in terms of spectral and angular dependencies, of the light transmission profiles of dry and wet sand-textured soils.

Acknowledgements

Thanks to my supervisor Gladimir Baranoski for his unwavering confidence. Petri and Spencer for all their help. The thesis readers, professors Daudjee and Alencar. Brad whose shoulders I stood on. And Simiao for sticking with me through this.

Table of Contents

List of Figures	vii
List of Tables	x
1 Introduction	1
2 Relevant Soil Characteristics	5
3 Investigation Framework	8
3.1 Selected Sand-Textured Soil Samples	8
3.2 In Silico Experimental Setup	10
3.3 Baseline <i>In Silico</i> Experiments	12
4 Results and Discussion	15
4.1 Dry State Experiments	15
4.2 Intermediate Water-Saturated State Experiments	19
4.3 Water-Saturated State Experiments	22
4.4 Set IV - Water Film Experiments	22
4.5 Conceptual and Practical Implications	27
4.6 Interdisciplinary Outlook	31
5 Conclusion and Future Work	33

References	36
APPENDICES	46
Alphabetical Index	56

List of Figures

1.1	Examples of landscapes formed by sand-textured soils.	2
2.1	A sand-textured soil (left) is composed of grains (right) immersed in a pore space. Iron oxides are often present as pure particles, mixed with the grains' core material (<i>e.g.</i> , quartz), or embedded in their coatings.	6
2.2	Diagrams (not to scale) illustrating distinct water saturation states (associated with the presence, or absence, of water in the pore space) of a given natural sand sample. For clarity purposes, only a relatively small number of grains (particles) are depicted in the diagrams. From left to right, dry state, intermediate water-saturated state, water-saturated state and dry state with the grains encapsulated by water films.	7
3.1	Comparisons of measured [59] and modeled reflectance curves obtained for the selected natural sand samples. From left to right: Australian dune, Peruvian beach, Californian outcrop and Saudi Arabian dune samples. The modeled-R curves were computed considering the values for the iron oxide parameters (ϑ_{hg} and ϑ_m) provided in Table 3.1, while the modeled-U curves were computed considering a $10\times$ reduction of these values. All curves were obtained considering an angle of incidence of 0°	13
4.1	Comparisons of modeled transmittance curves computed for the selected sand-textured soil samples, in a dry state ($S = 0$), considering the values assigned to their iron oxide parameters (ϑ_{hg} and ϑ_m) provided in Table 3.1, and distinct thicknesses (1.0, 1.1 and 1.2 <i>mm</i>). From top to bottom: Australian dune, Peruvian beach, Californian outcrop and Saudi Arabian dune samples. Left: angle of incidence of 0° . Right: angle of incidence of 45° . . .	16

4.2	Comparisons of modeled transmittance curves computed for the selected sand-textured soil samples, in a dry state ($S = 0$), considering a $10\times$ reduction in the values assigned to their iron oxide parameters (ϑ_{hg} and ϑ_m) provided in Table 3.1, and distinct thicknesses (1.0, 2.0 and 3.0 <i>mm</i>). From top to bottom: Australian dune, Peruvian beach, Californian outcrop and Saudi Arabian dune samples. Left: angle of incidence of 0° . Right: angle of incidence of 45°	17
4.3	Comparisons of modeled transmittance curves computed for the selected sand-textured soil samples, in an intermediate water-saturated state ($S = 0.5$), considering the values assigned to their iron oxide parameters (ϑ_{hg} and ϑ_m) provided in Table 3.1, and distinct thicknesses (1.0, 1.1 and 1.2 <i>mm</i>). From top to bottom: Australian dune, Peruvian beach, Californian outcrop and Saudi Arabian dune samples. Left: angle of incidence of 0° . Right: angle of incidence of 45°	20
4.4	Comparisons of modeled transmittance curves computed for the selected sand-textured soil samples, in an intermediate water-saturated state ($S = 0.5$), considering a $10\times$ reduction in the values assigned to their iron oxide parameters (ϑ_{hg} and ϑ_m) provided in Table 3.1, and distinct thicknesses (1.0, 2.0 and 3.0 <i>mm</i>). From top to bottom: Australian dune, Peruvian beach, Californian outcrop and Saudi Arabian dune samples. Left: angle of incidence of 0° . Right: angle of incidence of 45°	21
4.5	Comparisons of modeled transmittance curves computed for the selected sand-textured soil samples, in a water-saturated state ($S = 1$), considering the values assigned to their iron oxide parameters (ϑ_{hg} and ϑ_m) provided in Table 3.1, and distinct thicknesses (1.0, 1.1 and 1.2 <i>mm</i>). From top to bottom: Australian dune, Peruvian beach, Californian outcrop and Saudi Arabian dune samples. Left: angle of incidence of 0° . Right: angle of incidence of 45°	23
4.6	Comparisons of modeled transmittance curves computed for the selected sand-textured soil samples, in a water-saturated state ($S = 1$), considering a $10\times$ reduction in the values assigned to their iron oxide parameters (ϑ_{hg} and ϑ_m) provided in Table 3.1, and distinct thicknesses (1.0, 2.0 and 3.0 <i>mm</i>). From top to bottom: Australian dune, Peruvian beach, Californian outcrop and Saudi Arabian dune samples. Left: angle of incidence of 0° . Right: angle of incidence of 45°	24

4.7	Comparisons of modeled transmittance curves computed for the selected sand-textured soil samples, in a dry state ($S = 0$) with the grains encapsulated by water films, considering the values assigned to their iron oxide parameters (ϑ_{hg} and ϑ_m) provided in Table 3.1, and distinct thicknesses (1.0, 1.1 and 1.2 mm). From top to bottom: Australian dune, Peruvian beach, Californian outcrop and Saudi Arabian dune samples. Left: angle of incidence of 0° . Right: angle of incidence of 45°	25
4.8	Comparisons of modeled transmittance curves computed for the selected sand-textured soil samples, in a dry state ($S = 0$) with the grains encapsulated by water films, considering a $10\times$ reduction in the values assigned to their iron oxide parameters (ϑ_{hg} and ϑ_m) provided in Table 3.1, and distinct thicknesses (1.0, 2.0 and 3.0 mm). From top to bottom: Australian dune, Peruvian beach, Californian outcrop and Saudi Arabian dune samples. Left: angle of incidence of 0° . Right: angle of incidence of 45°	26

List of Tables

3.1	Parameter values used to characterize the sand-textured soil samples considered in this investigation. The texture of the samples is described by the percentages (%) of sand (s_a) and silt (s_i). The particle type distributions considered in the simulations are given in terms of the percentages (%) of pure (μ_p), mixed (μ_m) and coated (μ_c) grains. The parameter r_{hg} corresponds to the ratio between the mass fraction of hematite to ϑ_{hg} (the total mass fraction of hematite and goethite). The parameter ϑ_m represents the mass fraction of magnetite, which is assumed to appear as pure particles [4].	9
3.2	Average dimensions (given in mm) of the major axes m_a and m_i that respectively define the ellipsoids used to represent the sand-sized and the silt-sized particles forming the sand-textured soil samples considered in this investigation.	10
4.1	Ranges of light penetration depth (in mm , as defined in Section 3.2) computed for the selected natural sand samples considering the values assigned to their iron oxide parameters (ϑ_{hg} and ϑ_m) presented in Table 3.1. Specific ranges are provided for each water saturation state (dry ($S = 0$), intermediate water-saturated ($S = 0.5$), water-saturated ($S = 1$) and dry ($S = 0$) with the individual grains encapsulated by water films) and angle of incidence (0° and 45°) considered in this investigation.	28
4.2	Ranges of light penetration depth (in mm , as defined in Section 3.2) computed for the selected natural sand samples considering a $10\times$ reduction in the values assigned to their iron oxide parameters (ϑ_{hg} and ϑ_m) presented in Table 3.1. Specific ranges are provided for each water saturation state (dry ($S = 0$), intermediate water-saturated ($S = 0.5$), water-saturated ($S = 1$) and dry ($S = 0$) with the individual grains encapsulated by water films) and angle of incidence (0° and 45°) considered in this investigation.	29

B.1	RMSE values computed for the modeled curves, which were obtained using the SPLITS-2 model implementation (Appendix A), with respect to their measured counterparts [59].	55
-----	--	----

Chapter 1

Introduction

Computer simulations, or *in silico* experiments, have been recognized to be instrumental to resolve critical issues related to important remote sensing targets, notably vegetation, soil and snow cover, especially at a global scale (*e.g.*, monitoring of target status, prediction of environmentally-triggered changes and retrieval of specific target properties), in the quantitative remote sensing area [29, 30, 32, 39]. Similarly, the applied research described in this thesis aims to contribute to the increase of the fidelity to cost ratio of remote sensing applications and geoscience investigations involving naturally occurring sand-textured soils, commonly referred to as natural sands. To achieve this goal, we employed a computational platform significantly enhanced for this purpose during this work.

Sand-texture soils (Fig. 1.1) comprise over 20% of the planet's land surface [21]. During the last decades, they have become one of the primary focal points of remote sensing research (*e.g.*, [2, 3, 55, 58, 63]) and geoscience investigations (*e.g.*, [44, 51, 61]). This role is bound to become even more prevalent as aridification and desertification processes



Figure 1.1: Examples of landscapes formed by sand-textured soils.

elicited by climate change continue to have a negative impact on more than two billion people living in drylands [13]. Moreover, these soils may cover other important remote sensing targets such as arable fields and crops [1]. The high-precision remote monitoring of these targets requires reliable information about the depth from which the measured signal originates [20]. This information, in turn, is directly associated with these soils' light attenuation properties [66].

Besides their relevance for remote sensing application properties, the light attenuation properties of sand-textured soils are also central in applications with a strong geoscience component, *i.e.*, involving Earth's soil, mineral, water and energy resources, and their interrelationships at macroscopic (*e.g.*, erosion of coastal terrains) and microscopic (*e.g.*, physicochemical reactions on the surface of mineral grains) scales [46]. For example, the high-fidelity remote estimation of the depth at which light can penetrate natural sand layers can lead to more reliable predictions about the germination of stress-adapted seeds [12, 38, 69], particularly in arid landscapes. It also represents an important piece of data in geophysical studies relying on the optical dating [43] to predict changes in sand deposits

[56], specially those found in regions more vulnerable to environmental changes like coasts and deltas [18].

Light penetration in natural sands can be directly measured (in terms of transmittance) using a spectrophotometer [3, 12, 66, 69]. Alternatively, it can be indirectly gauged using the germination of light-sensitive seeds or the presence of growing algae as bioindicators [12, 20, 38, 69]. However, despite noteworthy efforts in these areas, the number of transmittance datasets available in the literature to date is still scarce. To make matters worse, besides covering a limited range of naturally-occurring sand-textured soils and water saturation states, these datasets have their generalization often hindered by experimental constraints.

Among these constraints, one can highlight the absence of key morphological features of natural sands (*e.g.*, the complex size distribution patterns of their constituent grains) in soil samples artificially prepared and mixed in the laboratory [3, 65], as well as the selection of samples with specific characteristics (*e.g.*, negligible presence of iron oxides) to facilitate the detection of transmittance signals [66]. Moreover, models (*e.g.*, [3, 66]) used in conjunction with these experimental efforts do not explicitly incorporate in their formulations the particulate nature of natural sands.

In this thesis, in order to overcome these constraints and strengthen the current knowledge about light penetration in natural sands, we employed a predictive computational (*in silico*) investigation framework that comprehensively takes into account the mineralogical and morphological characteristics of these materials, including their granular structure and composition. Using actual measured spectral datasets as references and sand characterization parameter values consistent with well-established soil information provided in the related literature, we performed controlled *in silico* experiments to evaluate the light

penetration depth of representative samples of natural sands subject to distinct water saturation states. Our *in silico* experiments were carried out considering the 400 to 1000 *nm* region of the light spectrum, which corresponds to spectral domain often employed in the remote assessment of natural sands' mineralogy (*e.g.*, [44, 61, 63]) and related geoscience processes (*e.g.*, [14, 33, 69]). The outcomes of our investigation demonstrate the importance of taking into account the presence of iron oxides when estimating the light penetration depth of these soils in the spectral region of interest, and provide a comprehensive picture about a broad range of factors affecting these estimations.

Our findings demonstrate that the presence of iron oxides in natural sands needs to be appropriately taken into account so that one can obtain reliable light penetration depth estimations for these soils. The outcomes of our controlled *in silico* experiments also provide a high-fidelity portrait of variations on their transmittance in response to changes in light incidence geometry and water saturation conditions.

The remainder of this thesis, whose preliminary findings have been the object of a conference publication [7], is organized as follows. In Chapter 2, we provide a concise review about soil characteristics relevant for our investigation. In Chapter 3, we describe our investigation framework. In Chapter 4, we present our findings, discuss their conceptual and practical implications, and examine their significance in a broader applied research context. Finally, in Chapter 5, we provide concluding remarks and outline directions for future research.

Chapter 2

Relevant Soil Characteristics

Soils are primarily composed of grains (particles) of weathered rocks immersed in a medium of air and water (the pore space) [15]. The fraction of the total volume of a soil sample not occupied by its constituent grains is defined as its porosity [16]. This quantity, in turn, is affected by the soil texture, *i.e.*, the proportion of sand-sized grains (particles with dimensions between 0.05 to 2.0 *mm*), silt-sized grains (particles with dimensions between 0.002 to 0.05 *mm*) and clay-sized grains (particles with dimensions smaller than 0.002 *mm*) forming the sample [47, 64], with coarse soils normally being less porous than finer soils [16]. On average, naturally-occurring sand-textured soils contain at least 85% sand-sized particles [64], and their porosity normally varies between 35 and 50% [15, 60].

The rocks forming the core (parent) material of the sand-textured soils' constituent grains are typically silicate minerals like quartz [41]. Trace amounts of impurities, notably iron oxides (*e.g.*, hematite, goethite and magnetite), can significantly affect the spectral signatures of these soils, particularly in the visible to near-infrared region between 400



Figure 2.1: A sand-textured soil (left) is composed of grains (right) immersed in a pore space. Iron oxides are often present as pure particles, mixed with the grains' core material (*e.g.*, quartz), or embedded in their coatings.

to 1000 nm , and their overall appearance (Fig. 2.1). In fact, these impurities are largely responsible for the color of these soils [22, 35, 50, 67].

Depending on the weathering process responsible for the formation of sand-textured soils, their core materials may occur as pure particles [17], coated particles [70] or mixed with impurities [50]. A particle coating is formed by a mineral (*e.g.*, kaolinite) matrix that may embed impurities [70]. These may also occur as pure particles [17].

The presence of water in the pore space of a natural sand sample can be quantified in terms of its degree of water saturation, denoted by S . This quantity corresponds to the probability of light encountering water while traversing the pore space of a given sand sample [35], and it can vary from zero (dry state) to one (water-saturated state).

There are also situations in which the grains of dry layers of natural sands, albeit immersed in a pore space filled with air, may be encapsulated by water films [55]. This may happen, for example, after the bulk of water in the pore space has been either drained via gravity or partially evaporated, leaving only the water films around the grains [47].

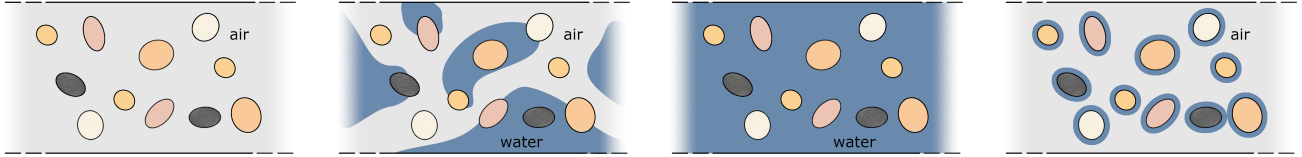


Figure 2.2: Diagrams (not to scale) illustrating distinct water saturation states (associated with the presence, or absence, of water in the pore space) of a given natural sand sample. For clarity purposes, only a relatively small number of grains (particles) are depicted in the diagrams. From left to right, dry state, intermediate water-saturated state, water-saturated state and dry state with the grains encapsulated by water films.

The diagrams presented in Fig. 2.2 illustrate these different patterns of water presence in natural sand samples. These patterns can significantly affect the optical properties of these soils [63, 69]. Consequently, they need to be properly taken into account by remote sensing applications targeting these soils (*e.g.*, aimed at the retrieval of information about their moisture content [2, 66]), as well as related geoscience investigations (*e.g.*, aimed at the assessment of their capability of eliciting seed germination and sustaining plant development [47, 11]).

Chapter 3

Investigation Framework

In this chapter, we initially present the natural sand samples employed in our investigation along with the data used in their characterization. We then concisely describe our *in silico* experimental setup and the different sets of controlled experiments performed in this work. Lastly, we review the outcomes of preliminary experiments performed to establish a baseline for our investigation.

3.1 Selected Sand-Textured Soil Samples

In our investigation, we considered samples from four natural sand deposits with distinct morphological and mineralogical characteristics, namely a red (hematite-rich) Australian dune, a dark (magnetite-rich) Peruvian beach site, a yellowish Californian outcrop and a red Saudi Arabian dune. These samples were employed in actual reflectance measurements [59] whose results were made available in the U.S. Army Topographic Engineering

Center (TEC) database [59] under the identifications TEC #10019201, TEC #10039240, TEC #19au9815 and TEC #13j9823, respectively.

In the characterization of the selected samples, we considered quartz as their core material and kaolinite as their coating matrix. In addition, we employed mean values for their porosity (0.425) [15], grain roundness (0.482) [68] and grain sphericity (0.798) [68]. The remaining parameter values used in their characterization are given in Table 3.1. In the absence of complete characterization datasets for the samples, these remaining values were also chosen from physically valid ranges reported in the literature [35] so that we could establish sound baselines for our investigation (Section 3.3).

samples	s_a	s_i	μ_p	μ_m	μ_c	r_{hg}	ϑ_{hg}	ϑ_m
Australian dune	90	10	0	50	50	0.80	0.012	0.0
Peruvian beach	95	5	50	0	50	0.375	0.05	0.17
Californian outcrop	92.5	7.5	50	25	25	0.25	0.042	0.0
Saudi Arabian dune	90	10	0	75	25	0.012	0.5	0.0

Table 3.1: Parameter values used to characterize the sand-textured soil samples considered in this investigation. The texture of the samples is described by the percentages (%) of sand (s_a) and silt (s_i). The particle type distributions considered in the simulations are given in terms of the percentages (%) of pure (μ_p), mixed (μ_m) and coated (μ_c) grains. The parameter r_{hg} corresponds to the ratio between the mass fraction of hematite to ϑ_{hg} (the total mass fraction of hematite and goethite). The parameter ϑ_m represents the mass fraction of magnetite, which is assumed to appear as pure particles [4].

Note that the percentages of the sand-sized and silt-sized particles depicted in Table 3.1 are employed to compute the dimensions of the samples' grains (Table 3.2) using a particle size distribution provided by Shirazi *et al.* [62]. Also, based on the samples' descriptions [59], we assumed the presence of clay-sized particles to be negligible.

samples	m_a	m_i
Australian dune	0.126	0.022
Peruvian beach	0.141	0.021
Californian outcrop	0.132	0.022
Saudi Arabian dune	0.126	0.022

Table 3.2: Average dimensions (given in mm) of the major axes m_a and m_i that respectively define the ellipsoids used to represent the sand-sized and the silt-sized particles forming the sand-textured soil samples considered in this investigation.

It also worth mentioning that Rinker *et al.* [59] did not report any presence of water or moisture when they performed the actual reflectance measurements employed as references in this investigation. Accordingly, we set the samples’ degree of water saturation to zero during the computation of the modeled reflectance curves presented in Section 3.3.

3.2 In Silico Experimental Setup

During our controlled *in silico* experiments, we have computed directional-hemispherical reflectance and transmittance curves using an enhanced version of the first-principles light transport model originally known as SPLITS (*Spectral Light Transport Model for Sand*) [35]. The stochastic formulation employed by this model includes parameters describing the morphology and mineralogy of the particles forming sand-textured soils, as well as the distribution of these particles within the pore space. To enable the reproduction and extension of our *in silico* experimental results, we have made an enhanced implementation of SPLITS (Appendix A), termed SPLITS-2 [28], available online [54], via a model distribution system [5], along with the supporting spectral datasets (*e.g.*, refractive index and extinction coefficient curves [53]) associated with the various minerals considered in this

investigation.

Each modeled radiometric curve was obtained using a virtual spectrophotometer [9] and casting 10^6 rays (per sampled wavelength) onto the natural sand samples. For the baseline reflectance experiments (Section 3.3), we considered the samples' thickness equal to 1 m , a default value that guarantees depth-invariant readings [20] like those obtained in the actual measurements [59]. For the transmittance experiments, we considered distinct values for the samples' thickness to evaluate their light transmission profiles as described below.

We have performed four sets of transmittance experiments (Section 4). These sets, henceforth referred to as I, II III and IV, correspond to the four distinct patterns of water presence depicted in Fig. 2.2, namely a dry state ($S = 0$), an intermediate water-saturated state ($S = 0.5$), a water-saturated state ($S = 1$) and a dry state ($S = 0$) with the grains encapsulated by water films, respectively. It is worth noting that the thickness of a water film depends on the sand sample's morphological characteristics, its previous water saturation state [47, 48] and environmental factors such as temperature [42]. For the purposes of our investigation, we assigned to the water film thickness a value of 5 μm , which is consistent with actual experiments involving the presence of water films encapsulating the grains of quartz-sand samples [48].

Each set of transmittance experiments, in turn, was composed of two subgroups of simulations, one considering the values assigned to the samples' iron oxide parameters (ϑ_{hg} and ϑ_m) provided in Table 3.1, and the other considering a $10\times$ reduction in these values. Furthermore, to increase our scope of observations, the simulations were carried out employing two distinct angles of light incidence (0° and 45°) and three different values

for the samples' thickness.

In order to complement our analysis of the samples' light transmission profiles, we have estimated their light penetration depth ranges with respect to each different testing condition stated earlier. The light penetration depth is defined as the depth at which the impinging light is reduced by $\geq 99\%$, yielding transmittance readings $\leq 1\%$ [20, 27]. Accordingly, in order to estimate these ranges, we have computed transmittance curves for the samples considering distinct values for their thickness. We varied these values in increments of 0.1 mm , which corresponds to the precision of light penetration depths provided for sand-textured soils in the related literature (*e.g.*, [12, 69]). The lower and upper limits of an estimated range are represented by the thickness values resulting in transmittance readings (in the 400 to 1000 nm region) below and above 1% , respectively. These limits were then reported (Section 4.5) as the light penetration depth range for each selected sample under each experimental condition considered in this investigation.

3.3 Baseline *In Silico* Experiments

We remark that, in the absence of complete characterization datasets for the selected natural sand samples [59], the values assigned to their parameters were chosen from physically valid ranges reported in the literature [35]. Thus, to assess the suitability of our choice of parameter values (Table 3.1), we computed reflectance curves (named modeled-R). We then compared these curves with the reflectance curves measured for the selected samples [59]. As it can be observed in Fig. 3.1, the modeled-R curves closely agree with their measured counterparts (a quantification of this agreement is presented in Appendix B).

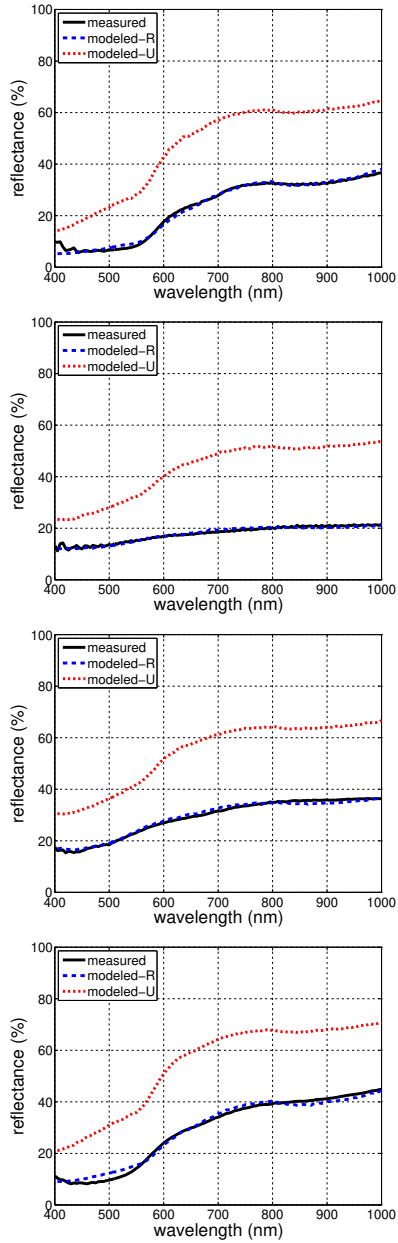


Figure 3.1: Comparisons of measured [59] and modeled reflectance curves obtained for the selected natural sand samples. From left to right: Australian dune, Peruvian beach, Californian outcrop and Saudi Arabian dune samples. The modeled-R curves were computed considering the values for the iron oxide parameters (ϑ_{hg} and ϑ_m) provided in Table 3.1, while the modeled-U curves were computed considering a $10\times$ reduction of these values. All curves were obtained considering an angle of incidence of 0° .

Accordingly, we employed the same parameter values in our transmittance experiments, the focus of our investigation. The results of these experiments are presented and discussed in Chapter 4.

Note that the iron oxide amounts depicted in Table 3.1, albeit realistic, correspond to a small fraction of the samples' total mass. Thus, one might assume that the iron oxides would have a low impact on the attenuation of light interacting with these samples. To examine the plausibility of this assumption, we also computed reflectance curves (named modeled-U) for both samples considering a $10\times$ reduction in the values of the iron oxide parameters (ϑ_{hg} and ϑ_m) depicted in Table 3.1. As it can be verified in plots presented in Fig. 3.1, although these curves are qualitatively similar to their measured counterparts, they have a distinctively higher magnitude. This illustrates the importance of properly accounting for the relatively small, but pivotal, presence of iron oxides when computing the reflectance of sand samples, particularly in the 400 to 1000 nm spectral domain [4]. The impact of this aspect on the samples' transmittance is systematically examined in the next section.

Chapter 4

Results and Discussion

In this chapter, we present the outcomes of our controlled *in silico* experiments involving the simulation of light transmission in the selected natural sand samples subject to four distinct water saturation states. We then discuss the conceptual and practical implications of our findings.

4.1 Dry State Experiments

The results of our *in silico* transmittance experiments considering the selected natural sand samples in a dry state ($S = 0$) are presented in Figs. 4.1 and 4.2. Examining the graphs depicted in Fig. 4.1, we note a nonlinear decrease in the samples' transmittance as their thickness is increased. Although the transmittance values tend to zero, their decrease becomes less accentuated with larger thickness values. Moreover, the transmittance values were higher at the longer wavelengths. This may be attributed to the relatively

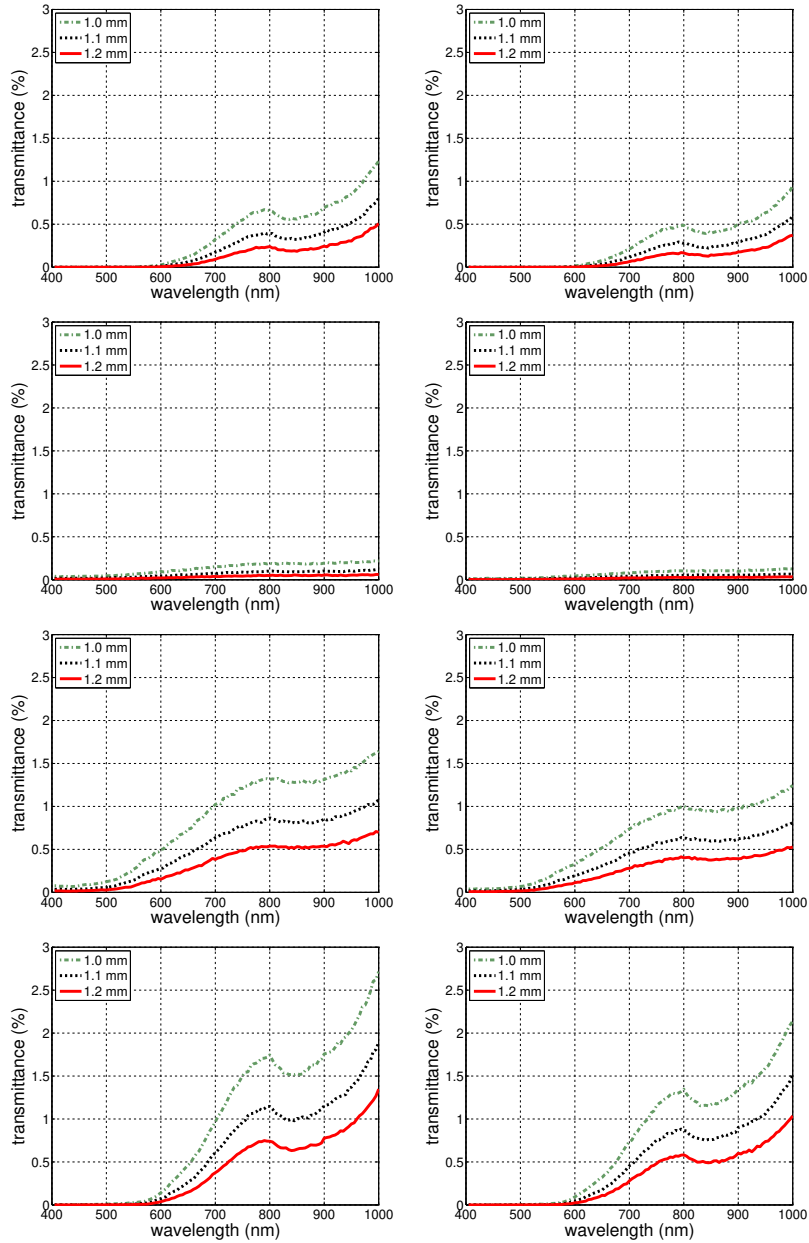


Figure 4.1: Comparisons of modeled transmittance curves computed for the selected sand-textured soil samples, in a dry state ($S = 0$), considering the values assigned to their iron oxide parameters (ϑ_{hg} and ϑ_m) provided in Table 3.1, and distinct thicknesses (1.0, 1.1 and 1.2 mm). From top to bottom: Australian dune, Peruvian beach, Californian outcrop and Saudi Arabian dune samples. Left: angle of incidence of 0° . Right: angle of incidence of 45° .

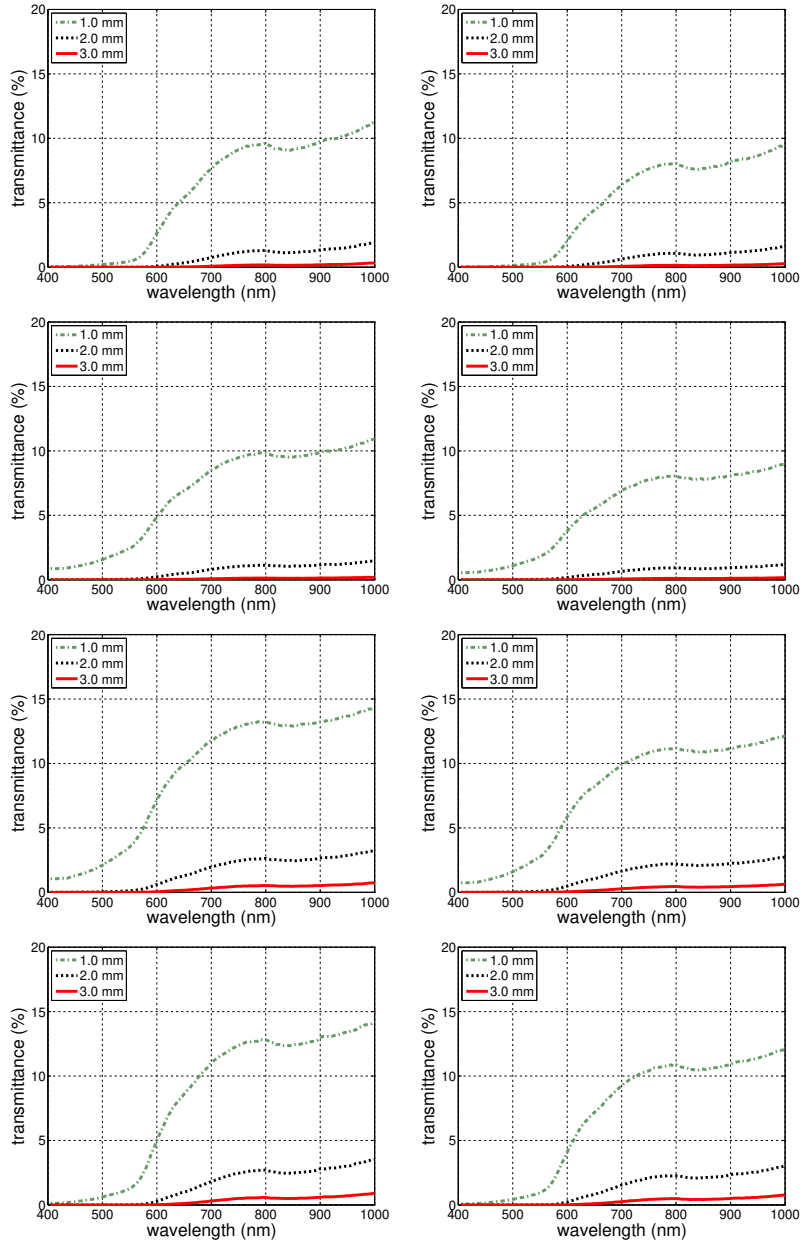


Figure 4.2: Comparisons of modeled transmittance curves computed for the selected sand-textured soil samples, in a dry state ($S = 0$), considering a $10\times$ reduction in the values assigned to their iron oxide parameters (ϑ_{hg} and ϑ_m) provided in Table 3.1, and distinct thicknesses (1.0, 2.0 and 3.0 mm). From top to bottom: Australian dune, Peruvian beach, Californian outcrop and Saudi Arabian dune samples. Left: angle of incidence of 0° . Right: angle of incidence of 45° .

low extinction coefficients of the iron oxides, notably hematite and goethite [35], at those wavelengths. These observations are consistent with the qualitative trends depicted in the spectrophotometric experiments performed by Woolley and Stoller [69] and Benvenuti [12] on colored sand samples. Also, in the graphs presented in Fig. 4.1, it can be verified that an increase in the angle of incidence, from 0° to 45° (with respect to the zenith), resulted in a slight, albeit noticeable, transmittance decrease, which has also been reported in the literature [66].

It has been suggested [12, 20, 65, 69] that, for a given particle size distribution, a lighter-colored (less absorptive) sand sample allows more and deeper light penetration than a darker-colored (more absorptive) one. However, to the best of our knowledge, no controlled experiments specifically performed to quantitatively examine this behaviour in natural sands have been reported in the literature to date. Hence, for comparison purposes, we repeated the transmittance experiments on the samples in a dry state considering a $10\times$ reduction in the values of their iron oxide parameters (ϑ_{hg} and ϑ_m) provided in Table 3.1. As expected, the resulting transmittance curves presented in Fig. 4.2 are significantly higher than those presented in Fig. 4.1. This aspect can undoubtedly be associated with the reduced attenuation of the light traversing samples characterized by uncommon lower amounts of iron oxides.

4.2 Intermediate Water-Saturated State Experiments

The results of our *in silico* transmittance experiments considering the selected natural sand samples in an intermediate water-saturated state ($S = 0.5$) are presented in Figs. 4.3 and 4.4. These results depict the same qualitative trends verified for the samples in a dry state (Set I). More specifically, one can observe the nonlinear decrease in transmittance following a linear increase in the samples' thickness, and the slight decrease in transmittance following an increase in the angle of incidence. In addition, one can also observe a similar substantial increase in transmittance when the sample's iron oxide contents are significantly reduced (Fig. 4.4).

The presence of water, however, resulted in higher transmittance readings, as shown in the graphs presented in Figs. 4.3 and 4.4, in comparison with the readings obtained for the samples in a dry state. This behaviour is consistent with actual experimental observations [45, 65, 69] on the transmittance of wet sand-textured soils. In the case of our experiments considering a $10\times$ reduction in the samples iron oxide contents, the presence of water also resulted in a noticeable dip in the 940 to 980 *nm* region (Fig. 4.4). This spectral feature is associated with a point of absorption maxima of water within this region [57]. By reducing the presence of iron oxides and having water in the samples' pore space, the light attenuation within this region becomes more dominated by the latter. This, in turn, elicits this feature which is characteristic of wet sand samples with negligible amounts of iron oxides [66].

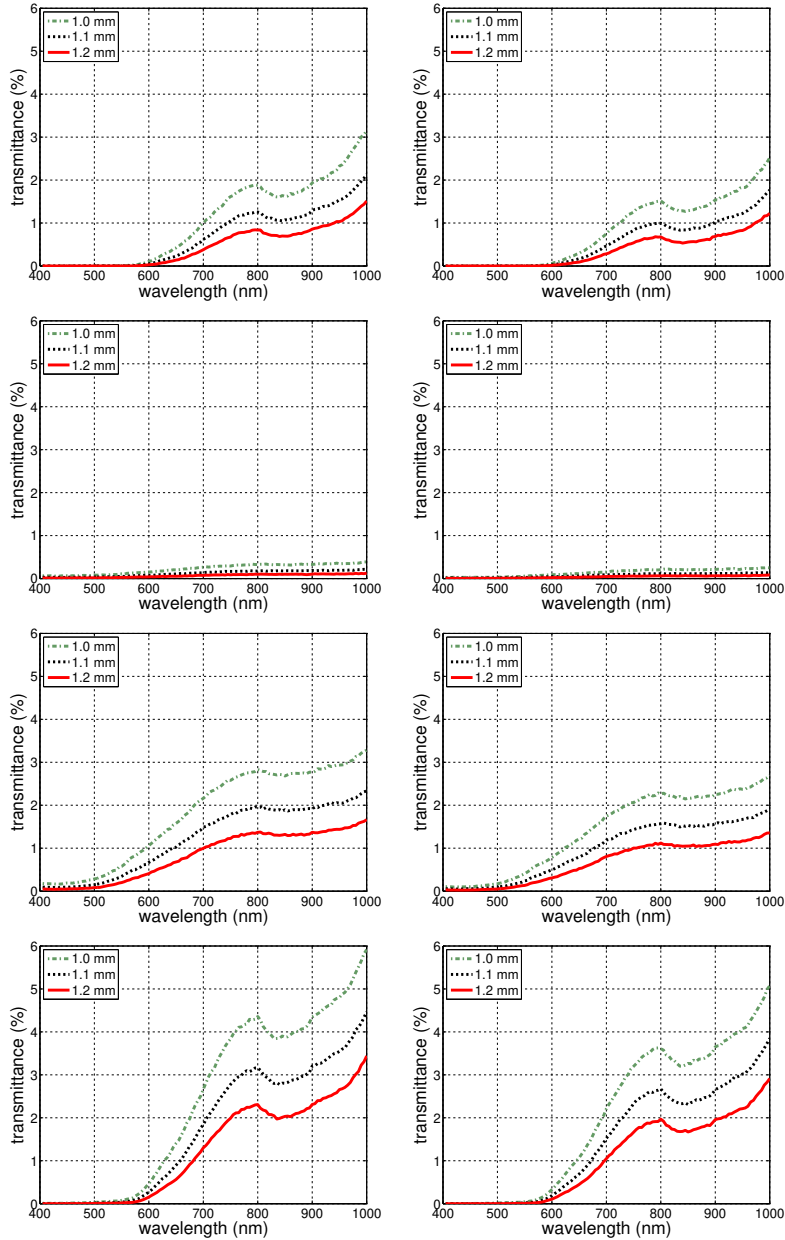


Figure 4.3: Comparisons of modeled transmittance curves computed for the selected sand-textured soil samples, in an intermediate water-saturated state ($S = 0.5$), considering the values assigned to their iron oxide parameters (ϑ_{hg} and ϑ_m) provided in Table 3.1, and distinct thicknesses (1.0, 1.1 and 1.2 mm). From top to bottom: Australian dune, Peruvian beach, Californian outcrop and Saudi Arabian dune samples. Left: angle of incidence of 0° . Right: angle of incidence of 45° .

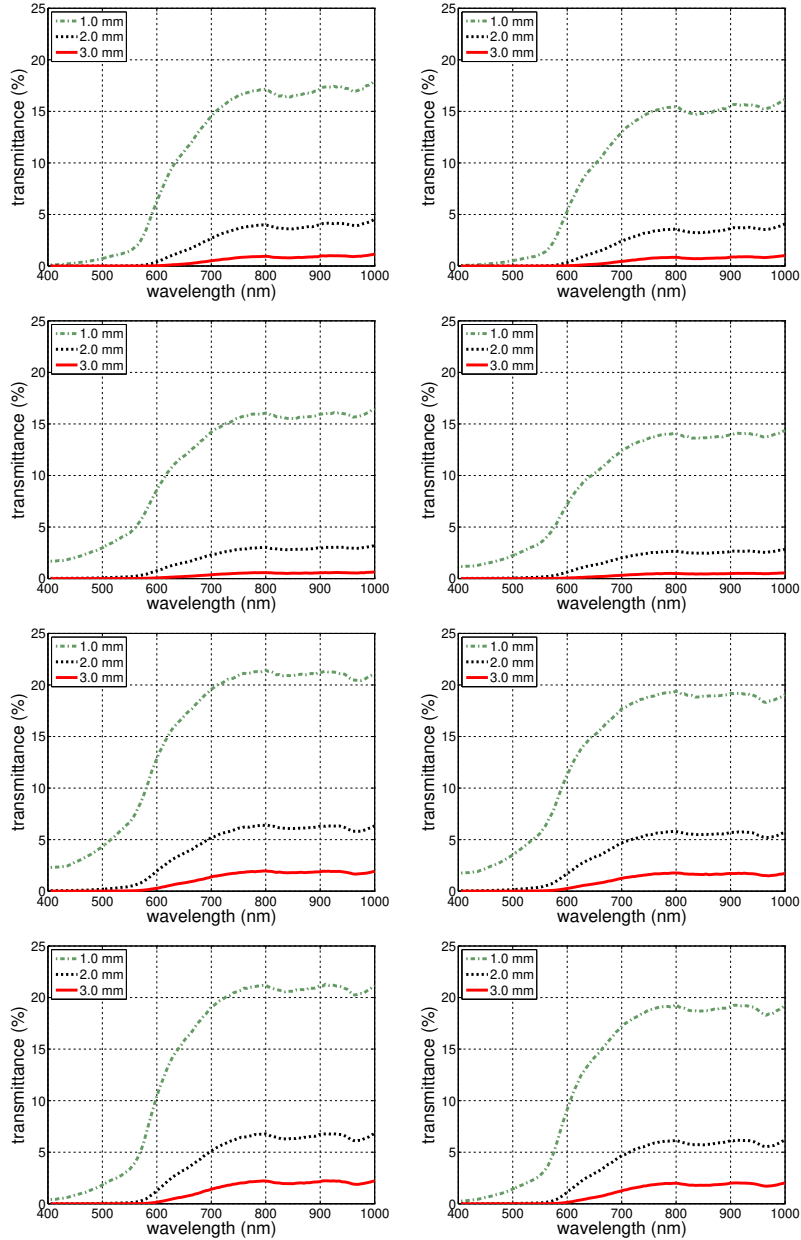


Figure 4.4: Comparisons of modeled transmittance curves computed for the selected sand-textured soil samples, in an intermediate water-saturated state ($S = 0.5$), considering a $10\times$ reduction in the values assigned to their iron oxide parameters (ϑ_{hg} and ϑ_m) provided in Table 3.1, and distinct thicknesses (1.0, 2.0 and 3.0 mm). From top to bottom: Australian dune, Peruvian beach, Californian outcrop and Saudi Arabian dune samples. Left: angle of incidence of 0° . Right: angle of incidence of 45° .

4.3 Water-Saturated State Experiments

The results of our *in silico* transmittance experiments considering the selected natural sand samples in a water-saturated state ($S = 1$) are presented in Figs. 4.5 and 4.6. Again, the qualitative trends observed in our previous sets of experiments were also verified when the presence of water was further increased in this set. Quantitatively, the resulting transmittance values were higher than those obtained for the samples in an intermediate water-saturated state (Figs. 4.3 and 4.4). Moreover, in the case of our experiments considering a 10× reduction in the samples iron oxide contents, the dip in the 940 to 980 *nm* region became more accentuated as depicted in Fig 4.6.

4.4 Set IV - Water Film Experiments

The results of our *in silico* transmittance experiments considering the selected natural sand samples in a dry state ($S = 0$) with the grains encapsulated by water films are presented in Figs. 4.7 and 4.8. Qualitatively, the same trends observed in the previous sets can also be observed in this set. Quantitatively, the results obtained in this set are similar to those obtained for Set II (Figs. 4.3 and 4.4).

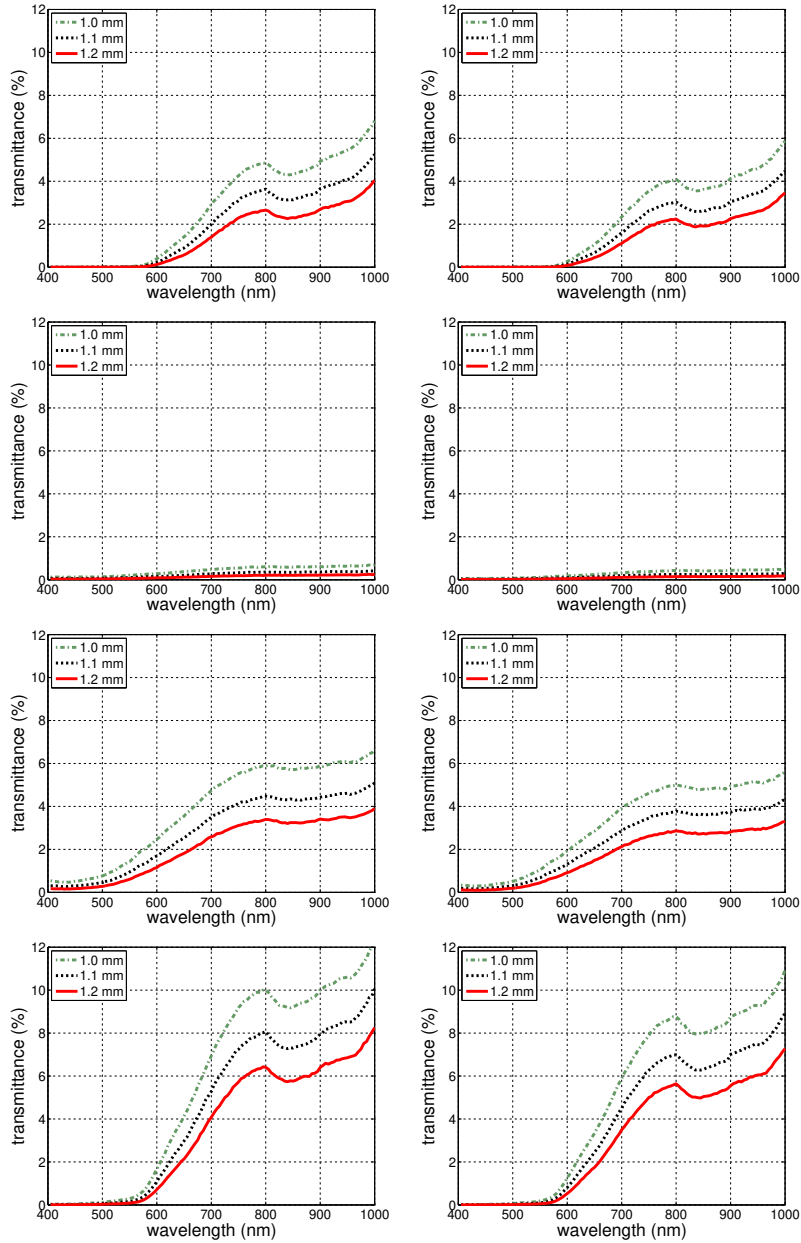


Figure 4.5: Comparisons of modeled transmittance curves computed for the selected sand-textured soil samples, in a water-saturated state ($S = 1$), considering the values assigned to their iron oxide parameters (ϑ_{hg} and ϑ_m) provided in Table 3.1, and distinct thicknesses (1.0, 1.1 and 1.2 mm). From top to bottom: Australian dune, Peruvian beach, Californian outcrop and Saudi Arabian dune samples. Left: angle of incidence of 0° . Right: angle of incidence of 45° .

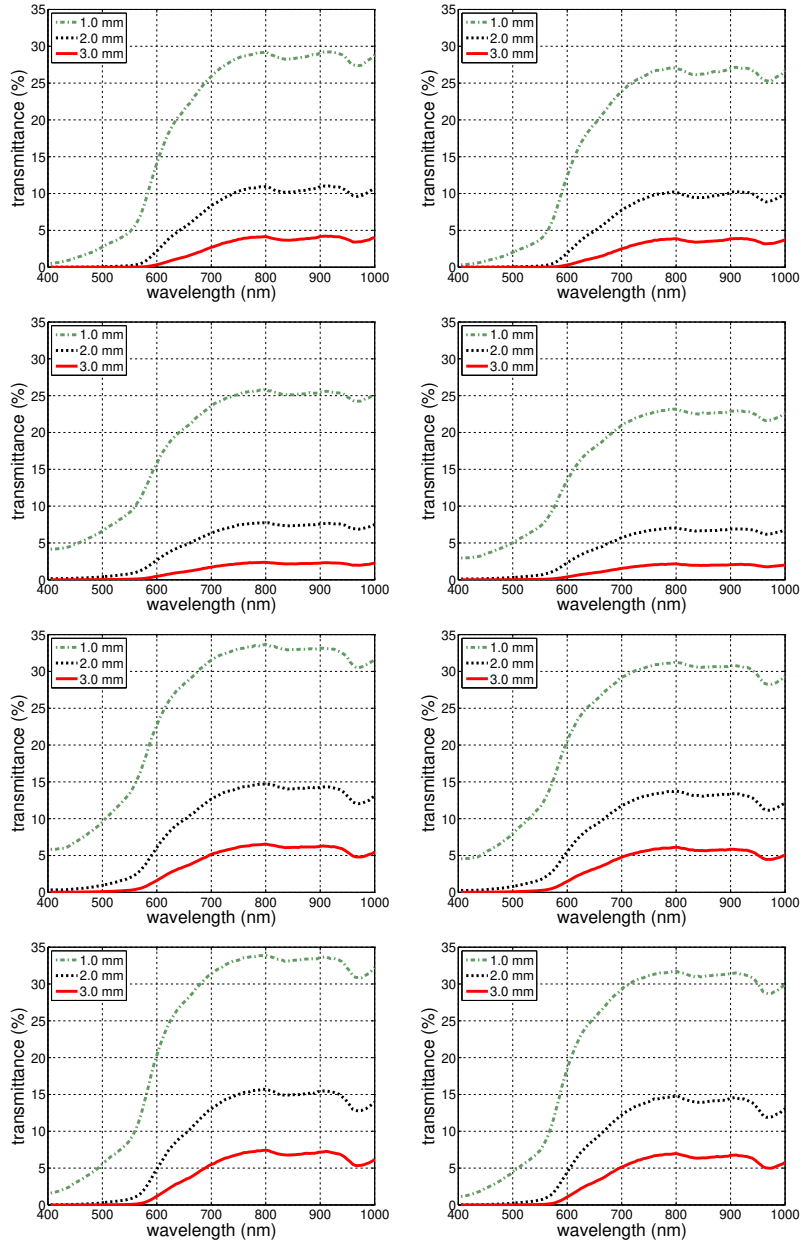


Figure 4.6: Comparisons of modeled transmittance curves computed for the selected sand-textured soil samples, in an water-saturated state ($S = 1$), considering a $10\times$ reduction in the values assigned to their iron oxide parameters (ϑ_{hg} and ϑ_m) provided in Table 3.1, and distinct thicknesses (1.0, 2.0 and 3.0 mm). From top to bottom: Australian dune, Peruvian beach, Californian outcrop and Saudi Arabian dune samples. Left: angle of incidence of 0° . Right: angle of incidence of 45° .

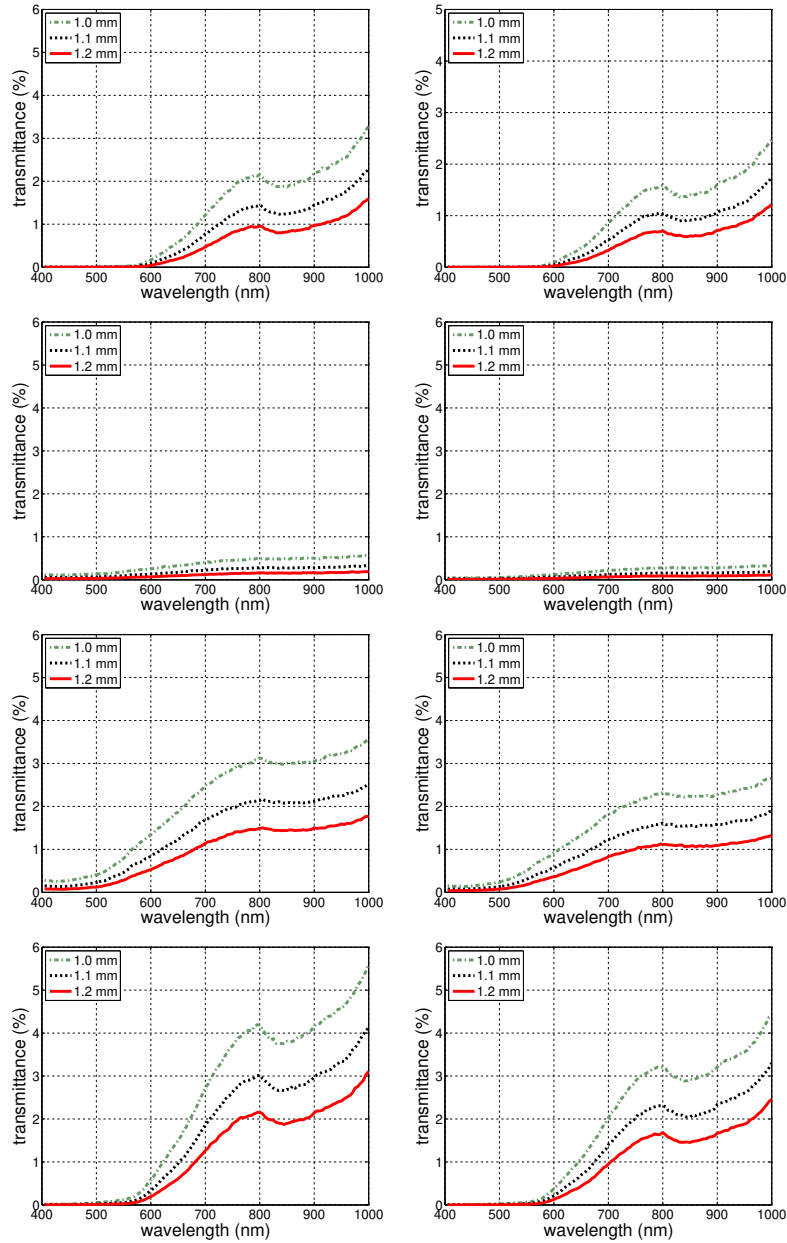


Figure 4.7: Comparisons of modeled transmittance curves computed for the selected sand-textured soil samples, in a dry state ($S = 0$) with the grains encapsulated by water films, considering the values assigned to their iron oxide parameters (ϑ_{hg} and ϑ_m) provided in Table 3.1, and distinct thicknesses (1.0, 1.1 and 1.2 mm). From top to bottom: Australian dune, Peruvian beach, Californian outcrop and Saudi Arabian dune samples. Left: angle of incidence of 0° . Right: angle of incidence of 45° .

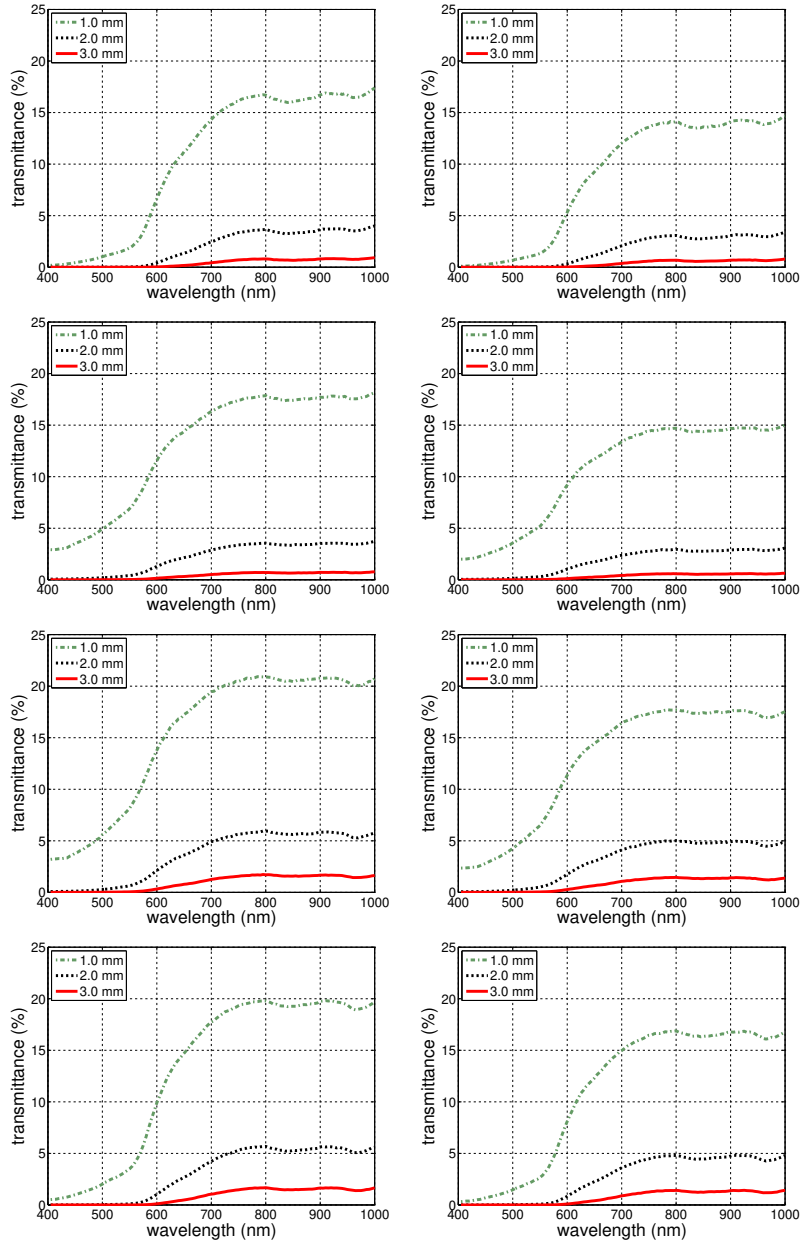


Figure 4.8: Comparisons of modeled transmittance curves computed for the selected sand-textured soil samples, in a dry state ($S = 0$) with the grains encapsulated by water films, considering a $10\times$ reduction in the values assigned to their iron oxide parameters (ϑ_{hg} and ϑ_m) provided in Table 3.1, and distinct thicknesses (1.0, 2.0 and 3.0 mm). From top to bottom: Australian dune, Peruvian beach, Californian outcrop and Saudi Arabian dune samples. Left: angle of incidence of 0° . Right: angle of incidence of 45° .

4.5 Conceptual and Practical Implications

The light penetration depth ranges computed for the selected samples considering the entire spectral region of interest (from 400 to 1000 nm) are provided in Table 4.1. For the samples in a dry state, a thickness between 1.2 to 1.3 mm was required to obtain transmittance values below 1% in the worst case (Saudi Arabian dune sample). We remark that the literature on this topic is scarce, particularly with respect to actual measured data, and direct comparisons are difficult to be performed in view of the limited descriptions of the samples used in the actual experiments. Nonetheless, our estimated ranges are consistent with values provided in related works. For instance, Woolley and Stoller [69] reported transmittance values (from 350 to 800 nm) below 2% for a depth of 1.1 mm in a dry natural sand sample. Also, Benvenuti [12] reported a light penetration depth of 1 mm in his experiments (from 400 to 800 nm) on a dry sample with 93% of its granular structure composed of sand-sized particles.

For the *in silico* experimental instances in which we accounted for the presence of water in the samples' pore space, the computed ranges, which are also presented in Table 4.1, indicated an increase in the samples' light penetration depth following an increase in their degree of water saturation. In the worst case (water-saturated Saudi Arabian dune sample), a thickness between 2.2 to 2.3 mm was required to obtain transmittance values below 1%. Such an increase in the light penetration depth was to be expected in view of the increase in transmittance elicited by the presence of water [20, 69].

samples	water saturation states							
	dry		intermediate		saturated		dry with water films	
	0°	45°	0°	45°	0°	45°	0°	45°
Australian dune	1.0 - 1.1	0.9 - 1.0	1.3 - 1.4	1.2 - 1.3	1.7 - 1.8	1.6 - 1.7	1.3 - 1.4	1.2 - 1.3
Peruvian beach	0.7 - 0.8	0.6 - 0.7	0.8 - 0.9	0.7 - 0.8	0.9 - 1.0	0.8 - 0.9	0.9 - 1.0	0.8 - 0.9
Californian outcrop	1.1 - 1.2	1.0 - 1.1	1.3 - 1.4	1.2 - 1.3	1.7 - 1.8	1.6 - 1.7	1.3 - 1.4	1.2 - 1.3
Saudi Arabian dune	1.2 - 1.3	1.2 - 1.3	1.6 - 1.7	1.5 - 1.6	2.2 - 2.3	2.2 - 2.3	1.5 - 1.6	1.5 - 1.6

Table 4.1: Ranges of light penetration depth (in mm , as defined in Section 3.2) computed for the selected natural sand samples considering the values assigned to their iron oxide parameters (ϑ_{hg} and ϑ_m) presented in Table 3.1. Specific ranges are provided for each water saturation state (dry ($S = 0$), intermediate water-saturated ($S = 0.5$), water-saturated ($S = 1$) and dry ($S = 0$) with the individual grains encapsulated by water films) and angle of incidence (0° and 45°) considered in this investigation.

samples	water saturation states							
	dry		intermediate		saturated		dry with water films	
	0°	45°	0°	45°	0°	45°	0°	45°
Australian dune	2.3 - 2.4	2.2 - 2.3	3.0 - 3.1	3.0 - 3.1	4.4 - 4.5	4.4 - 4.5	2.9 - 3.0	2.8 - 2.9
Peruvian beach	2.1 - 2.2	2.0 - 2.1	2.7 - 2.8	2.6 - 2.7	3.7 - 3.8	3.6 - 3.7	2.8 - 2.9	2.7 - 2.8
Californian outcrop	2.8 - 2.9	2.6 - 2.7	3.5 - 3.6	3.4 - 3.5	5.3 - 5.4	5.2 - 5.3	3.4 - 3.5	3.3 - 3.4
Saudi Arabian dune	2.9 - 3.0	2.8 - 2.9	3.7 - 3.8	3.6 - 3.7	5.6 - 5.7	5.6 - 5.7	3.4 - 3.5	3.2 - 3.3

Table 4.2: Ranges of light penetration depth (in mm , as defined in Section 3.2) computed for the selected natural sand samples considering a $10\times$ reduction in the values assigned to their iron oxide parameters (ϑ_{hg} and ϑ_m) presented in Table 3.1. Specific ranges are provided for each water saturation state (dry ($S = 0$), intermediate water-saturated ($S = 0.5$), water-saturated ($S = 1$) and dry ($S = 0$) with the individual grains encapsulated by water films) and angle of incidence (0° and 45°) considered in this investigation.

By examining the ranges presented in Table 4.1, one can also note that those depths computed considering the samples' grains encapsulated by water films were similar to those depths computed considering the samples in an intermediate water-saturated state. In the worst case (Saudi Arabian dune sample), a thickness between 1.5 and 1.6 *mm* was required to obtain transmittance values below 1%. We note that Woolley and Stoller [69] reported transmittance values (from 350 to 800 *nm*) below 1% for a depth of 2.2 *mm* in a moist sand sample composed of particles with a diameter between 0.3 to 0.5 *mm*. It has been reported that transmittance decreases following a reduction in the size of a sample's constituent grains [3, 12, 20]. Accordingly, for sand samples characterized by smaller particles, like those considered in this investigation (Table 3.2), one should expect a light penetration depth lower than that reported by Woolley and Stoller [69] .

The same trends outlined earlier were observed for the light penetration depth ranges computed considering a 10 \times reduction in the samples' iron oxide contents. However, the magnitude of these ranges, which are presented in Table 4.2, was substantially higher than that of the ranges presented in Table 4.1. In the worst case for the samples in a dry state (Saudi Arabian dune sample), a thickness between 2.9 to 3.0 *mm* was required to obtain transmittance values below 1%. Such higher values were also to expected due to an increase in transmittance following a substantial reduction in light attenuation associated

with a reduced presence of iron oxides [12]. Also, as expected, the presence of water further increased the samples' light penetration depths. In the worst case (water-saturated Saudi Arabian dune sample), a thickness between 5.6 to 5.7 *mm* was required to obtain transmittance values below 1%.

By comparing the ranges presented in Table 4.2 with their counterparts depicted in Table 4.1, one can verify the importance of accounting for the fact that the relatively small amounts of iron oxides found in natural sands can have a significant impact on their light penetration depth. Consequently, experiments employing samples with mineralogical characteristics that are not normally found in natural sand deposits are more suitable to provide qualitative rather than quantitative predictions about these soils. For example, recent spectrophotometric measurements [66] performed on a coarse (85% of the particles with a diameter between 0.5 and 1 *mm*) “white” sand samples with insignificant iron oxide amounts resulted in an upper bound for transmittance values (in the 400 to 1000 *nm* region) equal to 20% for a depth of 3 *mm*. This bound was substantially increased when water was added to the samples, a behaviour qualitatively congruent with the trends observed in our *in silico* experiments.

4.6 Interdisciplinary Outlook

We remark that the understanding and quantification of light penetration in sand-textured soils is essential for the successful application of hyperspectral remote sensing technologies to the solution of practical problems in a wide range of fields. In precision agriculture, for example, such technologies are being explored for weed mapping and control [51]. Many

species of plants are characterized by having seeds whose germination is influenced by the ratio of red ($\approx 645 \text{ nm}$) to infrared ($\approx 735 \text{ nm}$) impinging light [8]. These species include weeds that compete for natural resources, notably water and nutrients, with crop species. Their seeds are capable of responding to relatively small amounts of light, and vast populations of them are found in arable fields [14], notably buried in layers (of variable thickness) of natural sands that may cover these fields (*e.g.*, after being transported by aeolian events originating from arid landscapes [1]). Thus, new strategies to consistently reduce the proliferation of weed seeds in arable fields can certainly benefit from the use of remote sensing technologies for the reliable detection of these targets. The efficacy of such technologies, in turn, can be significantly enhanced by high-fidelity estimations of the light penetration depth of sand-textured soils containing these targets.

Clearly, the fidelity of estimations of the light penetration depth of natural sands depends on whether or not the actual morphological and mineralogical characteristics of these materials, as well as their water saturation states, are properly taken into account. Our findings, obtained using an *in silico* experimental framework centered on the particulate composition of natural sands, demonstrated not only the key role played by the iron oxides, but also how the light penetration depth of these soils can be largely overestimated if the presence of these minerals is overlooked.

Chapter 5

Conclusion and Future Work

In this thesis, we have investigated the interplay of key factors, namely the presence of iron oxides and the distinct patterns of water saturation, affecting the penetration of light in sand-textured soils. Using a first-principles *in silico* experimental setup, we were able to conduct a series of controlled transmittance experiments on different samples of naturally occurring sand-textured soils. Our findings demonstrate that the presence of iron oxides in these soils needs to be appropriately taken into account so that one can obtain high-fidelity estimations of their light penetration depths.

The outcomes of our controlled *in silico* experiments also provide a comprehensive portrait of variations on their transmittance in response to changes in light incidence geometry and water saturation conditions. This information, in turn, can contribute to the development of more cost-effective technologies for the remote monitoring of landscapes covered by natural sand deposits. Moreover, through its incorporation into multiscale geoscience models, it can also lead to more reliable predictions about the expansion of

these landscapes and the consequent systemic and abrupt changes in multiple attributes of surrounding ecosystems [13].

As future work, we intend to further explore phenomena connecting soil optical properties to the life cycle of plants. For example, the field capacity of a soil (approximately equivalent to an the intermediate degree of water saturation considered in this investigation) corresponds to the amount of water available for plant uptake until the permanent wilting point is reached [47]. This point, in turn, corresponds to the stage in which the water is held too firmly by the soil grains (forming encapsulating films created by surface tension between the water and the grains) for plants to extract it [47]. Although this water cannot directly influence plant growth, it can have an impact on the penetration of light affecting the germination of photoblastic seeds. Accordingly, we plan to investigate the effects of distinct water film characteristics on the light transmission profiles of moist sand-textured soils.

We also intend to examine the sensitivity of the natural sands' transmission profiles to the presence of other natural materials. For example, organic matter, or humus, can be found in relatively small amounts in these soils [15, 24]. This black substance, composed of animal and/or plant remains [15], is characterized by strong light attenuation properties, with low concentrations ($\approx 2\%$) leading to the masking of iron oxides' effects on the spectral responses of natural sands [10, 25]. Salts can also be found in these soils, notably forming arid and semiarid landscapes where evaporation exceeds precipitation [47]. Similarly, the presence of these substances can also affect the spectral responses of these soils.

Finally, we plan to extend our research to other soil types, notably clay-textured soils. Besides the macropores found in sand-textured soils, clayey soils are characterized by the

presence of micropores within peds formed by the aggregation of clay particles and the adhesion of iron oxides, organic matter and other substances (*e.g.*, carbonates) [47]. The combined effects of iron oxides and water on the penetration of light in soils with these morphological arrangements is likely to be quantitatively and qualitatively distinct from those verified in sand-textured soils. We intend to include the assessment of this hypothesis in our agenda of future investigations in this area.

The number of works aimed at the study of light penetration in natural sands is still relatively small. In many cases, researchers had to resort to the use of artificially-prepared sand samples and simplified experimental conditions due to logistics constraints. Given the relevant environmental and economical ramifications of this topic, we believe that the scientific community needs to provide a continuing support for efforts involving the measurement of soils' radiometric properties and the acquisition of fundamental data (*e.g.*, hyperspectral extinction coefficients and refractive indices) for their constituent materials. Moreover, it should also foment the pairing of these efforts with the use of computer simulation frameworks that can predictively reproduce and analyze the spectral responses of these soils without oversimplifying their intrinsic nature. These synergistic collaborations will be instrumental for the achievement of robust advances in remote sensing applications and geoscience investigations involving light interactions with soil.

References

- [1] M. Akhlaq, T.R. Sheltami, and H.T. Mouftah. A review of techniques and technologies for sand and dust storm detection. *Rev. environ. Sci. Biotechnol.*, 11:305–322, 2012.
- [2] A. Bablet, P.V.H. Vu, S. Jacquemoud, F. Viallefont-Robinet, S. Fabre, X. Briottet, M. Sadeghi, M.L. Whiting, F. Baret, and J. Tian. MARMIT: A multilayer radiative transfer model of soil reflectance to estimate surface soil moisture content in the solar domain (400-2500 nm). *Remote Sens. Environ.*, 217:1–17, 2018.
- [3] D. Bänninger and H. Flüher. Modeling light scattering at soil surfaces. *IEEE T. Geosci. Remote*, 42(7):1462–1471, 2004.
- [4] G.V.G. Baranoski, B.W. Kimmel T.F. Chen, and E. Miranda. Influence of sand-grain morphology and iron-oxide distribution patterns on the reflectance of sand-textured soils. *IEEE J-STARs*, 7(9):3755–3763, 2014.
- [5] G.V.G. Baranoski, T. Dimson, T.F. Chen, B.W. Kimmel, D. Yim, and E. Miranda. Rapid dissemination of light transport models on the web. *IEEE Comput. Graph.*, 32(3):10–15, 2012.

- [6] G.V.G. Baranoski, B.W. Kimmel, T.F. Chen, and E. Miranda. Simulating the spectral properties of iron-bearing regions of mars using the SPLITS model. In *2014 IEEE Geoscience and Remote Sensing Symposium*, pages 3013–3016. IEEE, 2014.
- [7] G.V.G. Baranoski, B.W. Kimmel, P. Varsa, and M. Iwanchyshyn. On the light penetration in natural sands. In *IEEE International Geoscience & Remote Sensing Symposium - IGARSS 2019*, pages 6933–6936, Yokohama, Japan, 2019.
- [8] G.V.G. Baranoski, B.W. Kimmel, P. Varsa, and M. Iwanchyshyn. Porosity effects on the red to far-red ratios of light transmitted in natural sands: Implications for photoblastic seed germination. In C.M.U. Neale and A. Maltese, editors, *Proc. of SPIE, Vol. 11149, Remote Sensing for Agriculture, Ecosystems, and Hydrology XXI, SPIE Remote Sensing*, pages 111490O–1–14, Strasbourg, France, 2019.
- [9] G.V.G. Baranoski, J.G. Rokne, and G. Xu. Virtual spectrophotometric measurements for biologically and physically-based rendering. *The Visual Comput.*, 17(8):506–518, 2001.
- [10] M.F. Baumgardner, L.F. Silva, L.L. Biehl, and E.R. Stoner. Reflectance properties of soils. *Adv. Agron.*, 38:1–43, 1985.
- [11] M.D. Bejarano, R. Villar, A.M. Murillo, and J.L. Quero. Effects of soil compaction and light on the growth of *Quercus pyrenaica Willd. (Fagaceae)* seedlings. *Soil Till Res.*, 110:108–114, 2010.
- [12] S. Benvenuti. Soil light penetration and dormancy of Jimsonweed (*Datura stramonium*) seeds. *Weed Sci.*, 43:389–393, 1995.

- [13] M. Berdugo, M. Delgado-Baquerizo, S. Soliveres, R. Hernández-Clemente, Y. Zhao, J.J. Gaitán, N. Gross, H. Saiz, V. Maire, A. Lehmann, M.C. Rillig, R.V. Solé, and F.T. Maestre. Global ecosystem thresholds driven by aridity. *Science*, 367:787–790, 2020.
- [14] D. Bliss and H. Smith. Penetration of light into soil and its role in the control of seed germination. *Plant Cell Environ.*, 8:475–483, 1985.
- [15] N.C. Brady. *The Nature and Properties of Soils*. Macmillan Publishing Co., New York, NY, USA, 8th edition, 1974.
- [16] N.C. Brady and R.R. Weil. *Elements of the Nature and Properties of Soils*. Prentice-Hall Inc., Upper Saddle River, NJ, USA, 2000.
- [17] D.C. Catling and J.M. Moore. The nature of coarse-grained crystalline hematite and its implications for the early environment of Mars. *Icarus*, 165:277–300, 2003.
- [18] E.L. Chamberlain. A bright approach to geochronology. *Phys. Today*, pages 74–75, September 2018.
- [19] T.F. Chen, G.V.G. Baranoski, B.W. Kimmel, and E. Miranda. Hyperspectral modeling of skin appearance. *ACM Transactions on Graphics*, 34(3):31, 2015.
- [20] A. Ciani, K.U. Goss, and R.P. Schwarzenbach. Light penetration in soil and particulate materials. *Eur. J. Soil. Sci.*, 56:561–574, 2005.
- [21] R.U. Cooke and A. Warren. *Geomorphology in Deserts*. University of California Press, Los Angeles, CA, USA, 1973.

- [22] R. Cornell and U. Schwertmann. *The Iron Oxides*. Wiley-VCH GmbH & Co. KGaA, Weinheim, Germany, 2nd edition, 2003.
- [23] J. Czarnecki, B. Radoev, L. Schramm, and R. Slavchev. On the nature of Athabasca oil sands. *Advances in Colloid and Interface Science*, 114:53–60, 2005.
- [24] J.A. Galantini, N. Senesis, G. Brunetti, and R. Rosell. Influence of texture on organic matter distribution and quality and nitrogen and sulphur status in semiarid Pampean grassland soils of Argentina. *Geoderma*, 123(1-2):143–152, 2004.
- [25] L.S. Galvão and I. Vitorello. Role of organic matter in obliterating the effects of iron on the spectral reflectance and colour of Brazilian tropical soils. *Int. J. Remote Sens.*, 19(10):1969–1979, 1998.
- [26] D. Hanselman and B. Littlefield. *Mastering MATLAB 6 A Comprehensive Tutorial and Reference*. Prentice Hall, Upper Saddle River, NJ, 2001.
- [27] M. Huang, M.S. Kim K. Chao, J. Qin, C. Mo, C. Esquerre, S. Delwiche, and Q. Zhu. Penetration depth measurement of near-infrared hyperspectral imaging light for milk powder. *Sensors*, 441(16):1–11, 2016.
- [28] M.Y. Iwanchyshyn, B.W. Kimmel, and G.V.G. Baranoski. Revisiting the SPLITS model: Towards an enhanced implementation. Technical Report CS-2020-01, D.R. Cheriton School of Computer Science, University of Waterloo, Canada, 2020.
- [29] S. Jacquemoud and S. Ustin. *Leaf Optical Properties*. Cambridge University Press, UK, 2019.

- [30] S. Jacquemoud and S.L. Ustin. Leaf optical properties: A state of the art. In *8th International Symposium of Physical Measurements & Signatures in Remote Sensing*, pages 223–332, 2001.
- [31] S. Jacquemoud, S.L. Ustin, J. Verdebout, G. Schmuck, G. Andreoli, and B. Hosgood. Estimating leaf biochemistry using prospect leaf optical properties model. *Remote Sens. Environ.*, 56:194–202, 1996.
- [32] Z. Jiao, A. Ding, A. Kokhanovsky, C. Schaafd, F. Bréone, Y. Dong, Z. Wang, Y. Liu, X. Zhang, S. Yin, L. Cui, L. Meij, and Y. Chang. Development of a snow kernel to better model the anisotropic reflectance of pure snow in a kernel-driven BRDF model framework. *Remote Sens. Environ.*, 221:198–209, 2019.
- [33] M.J. Kasperbauer and P.G. Hunt. Biological and photometric measurement of light transmission through soils of various colors. *Bot. Gaz.*, 149(4):361–364, 1988.
- [34] B.W. Kimmel. SPLITS: A spectral light transport model for sand. Master’s thesis, D.R. Cheriton School of Computer Science, University of Waterloo, Canada, 2005.
- [35] B.W. Kimmel and G.V.G. Baranoski. A novel approach for simulating light interaction with particulate materials: application to the modeling of sand spectral properties. *Opt. Express*, 15(15):9755–9777, 2007.
- [36] B.W. Kimmel and G.V.G. Baranoski. A compact framework to efficiently represent the reflectance of sand samples. *IEEE Transactions on Geoscience and Remote Sensing*, 47(11):3625–3629, 2009.

- [37] B.W. Kimmel and G.V.G. Baranoski. Simulating the appearance of sandy landscapes. *Computers & Graphics*, 34(4):441–448, 2010.
- [38] D. Koller, M. Sachs, and M. Negbi. Germination-regulation mechanisms in some desert seeds VIII *Artemisia monosperma*. *Plant Cell Physiol.*, 5:85–100, 1964.
- [39] S. Labarre, C. Ferrari, and S. Jacquemoud. Surface roughness retrieval by inversion of the Hapke model: A multiscale approach. *Icarus*, 290:63–80, 2017.
- [40] S.R. Van Leeuwen, G.V.G. Baranoski, and Bradley W Kimmel. Revisiting the CLBlood model: Formulation enhancements and online deployment. *Technical Report CS-2017-01, D.R. Cheriton School of Computer Science, University of Waterloo, Canada*, 2017.
- [41] D.J. Leu. Visible and near-infrared reflectance of beach sands: a study on the spectral reflectance/grain size relationship. *Remote Sens. Environ.*, 6(3):169–182, 1977.
- [42] W. Li, Y. Zhang, W. Wei, and Z. Gu. Discussions of some issues for wind blown sand flow simulation. *Procedia IUTAM*, 17:1190128, 2015.
- [43] O.B. Lian, D.J. Huntley, and S.A. Wolfe. Optical dating of eolian dune sand from Canadian prairies. *Geogr. Phys. Quatern.*, 56(2-3):191–202, 2002.
- [44] M.L. Manchanda, M. Kudrat, and A.K. Tiwari. Soil survey and mapping using. *Trop. Ecol.*, 13:287–294, 2002.
- [45] D.F. Mandoli, G.A. Ford, L.J. Waldron, J.A. Nemson, and W.R. Briggs. Some spectral properties of several soil types: implications for photomorphogenesis. *Plant Cell Environ.*, 13:287–294, 1990.

- [46] C.A. Manduca and Kim A. Kastens. Geoscience and geoscientists: Uniquely equipped to study Earth. *Geol. S. AM. S.*, 486:1–12, 2012.
- [47] A. McCauley, C. Jones, and J. Jacobsen. Basic soil properties. Technical Report Soil & Water, Management Module I, Montana State University, USA, 2005.
- [48] A. Mekonen, P. Sharma, and F. Fagerlund. Transport and mobilization of multi-wall carbon nanotubes in quartz sand under varying saturation. *Environ. Earth Sci.*, 71:3751–3760, 2014.
- [49] Z. Merali. ...ERROR ...why scientific programming does not compute. *Nature*, 467:775–777, 2010.
- [50] A. Mottana, R. Crespi, and G. Liborio. *Simon and Schuster’s Guide to Rocks and Minerals*. Simon and Schuster, Inc., New York, NY, USA, 1978.
- [51] D.J. Mula. Twenty five years of remote sensing in precision agriculture: Key advances and remaining knowledge gaps. *Biosyst. Eng.*, 114:358–371, 2013.
- [52] Natural Phenomena Simulation Group (NPSG). *Run SPLITS Online*. D.R. Cheriton School of Computer Science, University of Waterloo, Ontario, Canada, 2012. <http://www.npsg.uwaterloo.ca/models/splits.php>.
- [53] Natural Phenomena Simulation Group (NPSG). *Sand Data*. D.R. Cheriton School of Computer Science, University of Waterloo, Ontario, Canada, 2012. <http://www.npsg.uwaterloo.ca/data/sand.php>.

- [54] Natural Phenomena Simulation Group (NPSG). *Run SPLITS-2 Online*. D.R. Cherton School of Computer Science, University of Waterloo, Ontario, Canada, 2020. <http://www.npsg.uwaterloo.ca/models/splits2.php>.
- [55] D.L. Neema, A. Shah, and A.N. Patel. A statistical model for light reflection and penetration through sand. *Int. J. Remote Sens.*, 8(8):1209–1217, 1987.
- [56] J. Ollerhead. Light transmittance through dry, sieved sand: some test results. *Ancient TL*, 19(1):13–17, 2001.
- [57] K. F. Palmer and D. Williams. Optical properties of water in the near infrared. *J. Opt. Soc. Am.*, 64(8):1107–1110, 1974.
- [58] W. Philpot and J. Tian. Light transmission through a sand layer: modeling changes due to illumination direction. In U. Michel and K. Schulz, editors, *Proc. of SPIE, Vol. 10428, Earth Resources and Environmental Remote Sensing/GIS Applications VIII SPIE, Remote Sensing*, pages 104210T1–8, Warsaw, Poland, 2017.
- [59] J.N. Rinker, C.S. Breed, J.F. McCauley, and P.A. Corl. Remote sensing field guide – desert. Technical Report ETL-0588, U.S. Army Topographic Engineering Center, Fort Belvoir, VA, USA, September 1991.
- [60] J. Román-Sierra, J.J. Muñoz-Perez, and M. Navarro-Plus. Beach nourishment effects on sand porosity variability. *Coast. Eng.*, 83:221–232, 2014.
- [61] R.A.V. Rossel, E.N. Bui, P. de Caritat, and N.J. McKenzie. Mapping iron oxides and the color of Australian soil using visible-near-infrared reflectance spectra. *J. Geophys. Res.*, 115:F04031:1–3, 2010.

- [62] M.A. Shirazi, L. Boersma, and J.W. Hart. A unifying quantitative analysis of soil texture: Improvement of precision and extension of scale. *Soil Sci. Soc. Am. J.*, 52(1):181–190, 1988.
- [63] R.A. Shuman. Determination of beach sand parameters using remotely sensed aircraft reflectance data. *Remote Sens. Environ.*, 11:295–310, 1981.
- [64] Soil Sci. Division Staff. Soil survey manual. Technical Report USDA Handbook 18, Soil Conservation Service, United States Department of Agriculture, USA, 1993.
- [65] M. Tester and C. Morris. The penetration of light through soil. *Plant Cell Environ.*, 10:281, 1987.
- [66] J. Tian and W. Philpot. Spectral transmittance of a translucent sand with directional illumination. *IEEE T. Geosci. Remote*, 56(8):4307–4317, 2018.
- [67] J. Torrent, U. Schwertmann, H. Fetcher, and F. Alferez. Quantitative relationships between soil color and hematite content. *Soil Sci.*, 136:354–356, 1983.
- [68] M.J. Vepraskas and D.K. Cassel. Sphericity and roundness of sand in costal plain soils and relationships with soil physical properties. *Soil Sci. Soc. Am. J.*, 51(5):1108–1112, 1987.
- [69] J.T. Woolley and E.W. Stoller. Light penetration and light-induced seed germination in soil. *Plant Physiol.*, 61:597–600, 1978.
- [70] H. Wopfner and C.R. Twidale. Australian desert dunes: wind rift or depositional origin? *Aust. J. Earth Sci.*, 48:239–244, 2001.

- [71] D. Yim, G.V.G. Baranoski, B.W. Kimmel, T.F. Chen, and E. Miranda. A cell-based light interaction model for human blood. *Computer Graphics Forum*, 31(2):845–854, 2012.
- [72] X. Zheng, R. Zhang, and H. Huang. Theoretical modeling of relative humidity on contact electrification of sand particles. *Scientific Reports*, 4:4399, 2014.

APPENDICES

Appendix A:

SPLITS-2 Implementation

Since the development of the SPLITS model [35, 34], it has been used in a number of investigations in computer graphics and remote sensing (*e.g.*, [6, 36, 37]). We remark that this model employs an innovative approach for the stochastic simulation of light transport in particulate materials. This approach allows the direct simulation of light (ray) interactions with specific material constituents (*e.g.*, sand grain, cells and organelles) without having to explicitly store them. Accordingly, it has been incorporated into other first-principles models, like CLBlood (Cell-based model of Light interaction with whole Blood) [40, 71] and HyLIoS (Hyperspectral Light Impingement on Skin) [19], developed by our group.

It is a well-known fact that any computer simulation code, regardless of its complexity and the programming skills of the people responsible for its implementation, is subject to the occurrence of “bugs”. These apparently tiny errors (*e.g.*, a flipped minus sign) may not necessarily cause a simulation to break down, but they can have a significant impact on its results [49].

Within this context, our group has found out that it pays off to obtain a “fresh” version of a model’s code. That is, have it rewritten by researchers not involved in its original formulation and implementation. However, we also noted that, if such an undertaking can be carried out with the support of those that have been involved in the development of the model, the chances of amplifying problems instead of fixing them are mitigated.

This code rewriting strategy has been systematically employed by our group [5]. It has enabled us not only to filter out possible bugs in the implementations of our models, but also to increase their fidelity to cost ratio through the use of more efficient software resources. Moreover, it has also facilitated the maintenance and the incorporation of new features to our models since the revised code tends to be structured in a more straightforward manner.

These aspects have also served as a motivation for a project which had two main goals. The first was to revisit the model’s formulation and rewrite its code from a “fresh” standpoint. The second was to release an enhanced version of its implementation, henceforth referred to as SPLITS-2, for online deployment through our model distribution framework NPSGD (Natural Phenomena Simulation Group Distributed) [5].

In this appendix, we concisely present refinements performed in the model’s implementation in order to completely align it with the model’s original formulation while preserving its predictive capabilities. More precisely, we identify the implementation problems, briefly explain their underlying causes and state how we fixed them. Note that, in this appendix, we address specific code modifications employed in the *in silico* experiments described in this thesis. The reader interested in more information about these modifications and other enhancements is referred to the document [28] describing the project leading to the deployment of SPLITS-2.

Non-Fixed Soil Texture Issue

Recall that soil samples are normally composed of particles (grains) of weathered rock immersed in a medium of air and water (the pore space). They are classified by assigning individual particles to classes according to their size. For example, the United States Department of Agriculture (USDA) defines three soil classes, namely sand, silt, and clay, from the largest to the smallest particles [35]. The relative masses of each component are then compared to determine the texture of a soil sample (*e.g.*, 85% sand-sized particles and 15% silt-sized particles). Also recall that, within the SPLITS formulation, the dimensions of the particles within each texture class are determined using a particle size distribution provided by Shirazi *et al.* [62].

When running a simulation using the original implementation of the model available for online use [52], henceforth referred simply as SPLITS, one can choose from a fixed set of six soil textures that will guide the size distribution of the particles within each class. These distributions are precomputed using MATLAB [26] scripts, and saved in files that do not change between model runs.

The enhanced model implementation, termed SPLITS-2, incorporates this precomputation as part of the model run framework. This means that the user can input any desired soil texture. The performance overhead is minimal. In fact, the computation of the particle size distribution can be performed fast enough to allow an interactive visualization of the process [28].

Particle Size Issue

While examining the SPLITS implementation, we noticed an error associated with the generation of the particles. In Listing A.1, we provide a code fragment showing how the size of the particles were generated by SPLITS. In this code fragment, the result of the sampling size distribution, `(m_size_warp)(Random::seed1())`, is passed directly to the semi-major axis of the spheroid, denoted by c . However, the result of the sampling size distribution corresponds to the entire major axis, denoted by s in Section 6.2.5 of the original publication describing SPLITS [34], *i.e.*, $s = 2c$. In order to correct this mistake, we simply divided c by 2.

```
70 Scalar c = (*m_size_warp)(Random::seed1());  
71 Scalar a = sphericity * sphericity * c;  
72 return new SpheroidParticle(a, c, Point3::Origin, axis);
```

Listing A.1: Code fragment inside `generate()` in `RandomSpheroidParticleGenerator.cpp`.

Coated Particles Issue

We remark that three types of particles, namely, pure, mixed and coated, are considered in the model's formulation. A mixed particle is made of two materials combined together using the Maxwell Garnet equation [35, 34]. Lastly, a coated particle is simulated as a pure particle with a layer (whose thickness is proportional to the particle size [35, 34]) formed by a distinct mineral matrix (possibly embedding impurities like iron oxides) around it.

Here the issue was a variable being passed by reference to different parameters employed

by a function used in the simulation of light scattering by a particle coating. One of the parameters was the output direction and the other the input direction. Thus, when the coating light scattering function set the output direction, it unintentionally also set the input direction to this value.

This was a problem because the function checked for an edge case where the light ray should have been reflected, when in fact it was not. However, since the input direction was modified, this edge case was detected more often than it should. We note that the edge case handling procedure set the output ray to a uniform random hemispherical direction [28].

While finding this bug was difficult, fixing it was not. All that was required was to make sure that the input and output direction were different variables when calling the function.

We remark that in the deployed version of SPLITS-2 [54], the percentages of mixed, pure, and coated particles are to be selected by the user, instead of being limited to a fixed number of choices like in the version of SPLITS available for online use [52].

Water Saturation Randomization Enhancement

In the SPLITS formulation, every time a ray enters the pore space (*e.g.*, after interacting with a particle), the traversing medium (water or air) is stochastically decided based on the water saturation parameter (S between 0 and 1).

This means that for a non-coated particle the pore space is randomized when the ray

tries to leave its core. In the case of coated particles, this means that the pore space is randomized when a ray exits the uppermost layer of coating. A concrete example: a ray is about to leave a particle and the soil has 10% water saturation ($S = 0.1$). This means, that each time the ray enters the pore space, there is a 10% chance of it being water and a 90% chance of being air (or vacuum).

In SPLITS-2, we have slightly modified this algorithm. More precisely, the medium changes only when the location of the ray does. The location is relevant because the distances in the coating are assumed to be small, *i.e.*, the ray does not deviate from its entry point to its exit point. This means that, when the ray is inside the coating, the pore medium is fixed as all the points within the coating are considered to be one point on the particle.

Incorporation of Water Film around Particles

Recall that the particles of dry sand layers ($S = 0$), albeit immersed in a pore space filled with air, may be encapsulated by water films [47]. In this case, the pore space may have been previously occupied and/or traversed by water, which has either percolated to underneath layers or partially evaporated, leaving only water films around the particles [47]. Related investigations in this area [23, 47] indicate that the thickness of a water film encapsulating a particle is likely to be independent of the particle size.

In the SPLITS-2 implementation, we have incorporated the possibility of having water films around the particles. The value assigned to the film thickness is selected by the user from physically-valid ranges reported in the related literature. This procedure matches

the procedures employed in other simulations and analyses involving particulate materials [48, 72]. Moreover, it allows the users to directly control the water film thickness and assess its effects on sand samples subject to varying environmental conditions.

Appendix B:

Root Mean Square Errors

In this appendix, for completeness, we provide root mean square error (RMSE) values computed for the modeled reflectance curves with respect to their measured counterparts (Section 3.1). These RMSE values were calculated using the following expression:

$$\text{RMSE} = \sqrt{\frac{1}{N} \sum_{i=1}^N (\rho_a(\lambda_i) - \rho_b(\lambda_i))^2}, \quad (\text{B.1})$$

where ρ_a and ρ_b respectively correspond to measured and modeled directional-hemispherical reflectance values, and N is the total number of wavelengths sampled with a 5 *nm* resolution.

The resulting RMSE values are presented in Table B.1. It is worth mentioning that there is an accepted understanding [31] that RMSE values below 0.03 indicate good spectrum reconstruction, notably for remote sensing applications.

samples	RMSE
Australian dune	0.0068
Peruvian beach	0.0132
Californian outcrop	0.0076
Saudi Arabian dune	0.0051

Table B.1: RMSE values computed for the modeled curves, which were obtained using the SPLITS-2 model implementation (Appendix A), with respect to their measured counterparts [59].

As it can be verified in Table B.1, the resulting RMSE values are below 0.015. This indicates that the modeled reflectance curves obtained using SPLITS-2 closely agree with their measured reflectance curves provided by Rinker *et al.* [59].

Alphabetical Index

- agriculture, [31](#)
- aridification, [1](#)
- bioindicators, [3](#)
- clay-sized grains, [5](#)
- coating matrix, [6](#)
- desertification, [1](#)
- drylands, [2](#)
- experimental constraints, [3](#)
- geoscience, [1](#)
- geoscience processes, [4](#)
- germination, [2](#)
- granular structure, [3](#)
- impurities, [5](#)
- interdisciplinary, [31](#)
- iron oxide, [3](#)
 - goethite, [5](#)
 - hematite, [5](#)
 - magnetite, [5](#)
- kaolinite, [6](#)
- light
 - angle of incidence, [11](#)
 - attenuation, [2](#)
 - penetration, [3](#)
 - penetration depth, [4](#)
 - reflectance, [8](#)
 - transmittance, [3](#)
 - transport model, [10](#)
 - wavelength, [11](#)
- macropore, [34](#)

micropore, 35

model distribution system, 10

morphological features, 3

ped, soil particle aggregates, 35

sand-sized grains, 5

silt-sized grains, 5

soil

- artificially prepared, 3
- porosity, 5
- texture, 5

spectrophotometer, 3

sphericity, 9

SPLITS, 10

SPLITS-2, 10

water, 2

- film, 6
- moisture, 7
- saturation, 3